

COMPUTATIONAL STUDY OF CANTILEVERED PLATE IN HIGH SPEED AXIAL FLOW

Kevin McHugh¹, Philip Beran¹, Earl Dowell²

¹Air Force Research Laboratory Wright-Patterson Air Force Base, OH, USA kevin.mchugh.3@us.af.mil philip.beran@us.af.mil

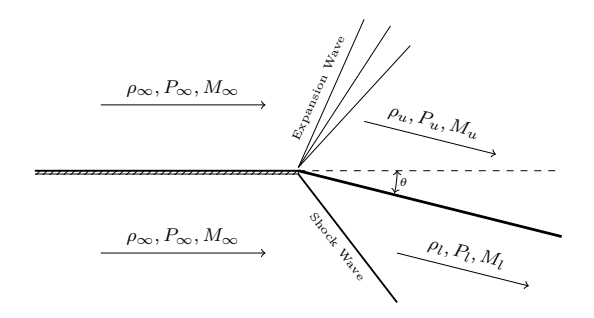
> ²Duke University Durham, NC, USA earl.dowell@duke.edu

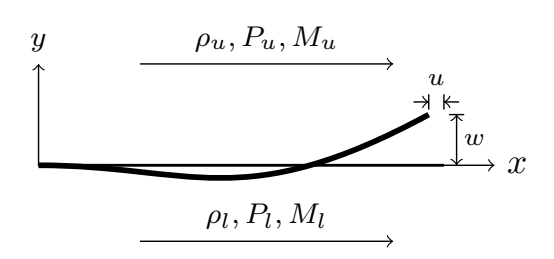
Abstract: A cantilevered plate at an angle of attack in axial high speed flow represents a prototypical control surface. Using a computationally efficient modal structural model coupled with a novel enhanced piston theory aerodynamic method, a nonlinear aeroelastic model is developed. Results presented include pre-flutter stable steady state solutions, flutter points, and post-flutter limit cycle oscillations. Because of the computationally efficient methodology, many simulations can be run to define sensitivities to mathematical modeling, model parameters, and numerical methods.

1 INTRODUCTION

Aeroelasticity of thin plates in high speed flow is currently generating much research interest. Recently, Spottswood et al. [1] have conducted experimental tests of a thin plate clamped on all four sides subjected to high speed flow, and have demonstrated nonlinear limit cycle oscillations as well as buckling behavior. Freydin et al. [2] modeled a similar system of a clamped plate with thermal stresses. In addition, Currao et al. have measured experimental pressures on and deflections of a cantilevered plate in high speed flow well below the flutter boundary with [3] and without [4] a shock impinging on the plate. The cantilevered configuration is of interest for modeling engineering structures such as trailing edge control surfaces on high speed aircraft. The present authors have developed and published a model which predicts the dynamics of a high speed cantilevered plate with no angle of attack in axial high speed flow undergoing post-flutter limit cycle oscillations (LCO) [5]. Presented here is the case with a trailing edge cantilever at an angle of rotation. Although the geometry in this case is simplified significantly from a flight-worthy control surface, the investigation of clamped-free boundary conditions of a thin, flat plate offers valuable insights into the fluid-structure interaction, stability, and effectiveness of these more complex systems.

This study is motivated mainly by two preliminary studies from the University of New South Wales. In the study by Currao et al. [4], the researchers examined a flexible cantilevered plate which was angled into high speed flow. At the leading edge corner, a shock wave was formed. The study compared an experiment, a high-fidelity computational fluid dynamics (CFD) technique, and a low-fidelity piston theory technique. Capturing the shock structure in CFD software proved computationally difficult and physically tedious due to meshing issues, with the researchers stating "The convergence of the simulation was extremely sensitive to the shape of the o-grid at the stagnation point...It was extremely challenging if not generally impossible, to align perfectly a strong (curved) shock with the mesh grid." They did, however, prove that





- (a) Schematic of full system including control surface hinge point and corresponding wave patterns
- (b) Schematic of aeroelastic system downstream of the hinge and expansion and shock waves

Figure 1: Schematics of the system illustrating (a) the full system and (b) the flexible trailing edge plate

the lower-fidelity piston theory was accurate to predict pressures on the plate in this type of configuration.

In a second publication by Currao et al. [3], the team examined the aeroelastic response to a plate in high speed flow with no angle of attack but rather an impinging shock wave. Again they compare piston theory to CFD and experiment with good accuracy. They also quantify flap efficiency, i.e. the moment acting on the control surface hinge compared to that from an ideal flap.

Motivated by these two studies indicating that piston theory can be used to examine high speed aeroelastic response, and propelled by the influx of new high speed research, we present theory and modeling to predict dynamics of control surfaces in high speed flows. The schematic for this case is shown in Fig. 1. The system consists of a flexible control surface connected to a rigid wing via a hinge and it is assumed that the hinge is perfectly rigid at each evaluation with no free-play or other nonlinearities. The aeroelastic behavior of the control surface is analyzed at several different values of control surface rotation angle θ . For any nonzero value of θ , we assume that there is a weak shock wave (resulting in > Mach 1 flow downstream) on one side and an expansion wave on the other, as shown in the diagram.

Because the streamlines of the flow turn with the angle θ , the control surface itself can be evaluated as if there were no angle of attack after accounting for a steady pressure differential due to the shock behavior. The system is shown in Fig. 1(b). And because the flow is high speed on both the top and bottom of the wing, we can enlist piston theory as our aerodynamic theory. These two assumptions significantly simplify our analysis. The structural theory will be the nonlinear inextensible beam theory, owing to the assumption that there is no torsion acting on the surface. Recent advances by the authors and colleagues in nonlinear beam and plate theory demonstrate a capability to model the responses of these structures with high computational efficiency [6–11]. Most recently, it has been shown that a model which couples the inextensible beam model with a piston theory aerodynamic forcing model can be used to predict aeroelastic behavior of a cantilever in high speed flow without any control surface rotation [5].

In the present paper, a new form of piston theory recently introduced by the authors [5] is used. Because the cantilevered conditions allow for large deflections of the structure, a new geometric modification to piston theory has been introduced. With use of the parameter $\beta(x)$ —the angle of the beam with respect to its undeformed datum—the pressure is always applied normal to the instantaneous shape of the beam.

The present model then includes several nonlinearities: two structural and several aerodynamic. The effects of the structural geometric nonlinearities alone have been reported previously by the authors [10,11], and the aerodynamic nonlinearities have been explored for the case with no

initial control surface rotation [5]. However, the aerodynamic nonlinearities for the case with an initial rotation are novel because of the inclusion of a steady pressure differential due to leading edge shock behavior as well as the inclusion of second order piston theory terms. The interplay among the nonlinearities proves to be interesting and important. It is also found that third order nonlinear piston theory predicts a significantly higher limit cycle amplitude than the first order linear theory, while second order piston theory is negligible for small control surface rotations.

Also note that when modeling any physical system and certainly a fluid-structural (aeroelastic) system, it is important to study the sensitivity of the results to different model attributes. Here we identify three types of sensitivities which are significant to this work. Type 1 is the sensitivity to the mathematical model of the physical system. How do the results change when new mathematics are introduced to the system? Type 2 is the sensitivity to the parameters that appear in the mathematical model or which are considered in the design of an experimental model. How do the results change based on varying geometric or material properties of the structure or the freestream flow properties? Type 3 is the accuracy of the numerical methods employed to extract solutions from the mathematical model. This is typically measured by performing a convergence study. Each of these is considered in the present paper.

The goals are to show the effectiveness of a computationally efficient modal aeroelastic model to predict behavior of and gain insight into the physics of simple, yet relevant aeroelastic systems. Because no high speed cantilevered plate wind tunnel tests have been performed near or beyond the flutter speed, this model will serve as the baseline for predicting aeroelastic structural deformations. Information such as moment on the hinge and maximum plate deflection will be of interest for experimentalists seeking to validate these results.

2 EQUATIONS OF MOTION

The equations of motion for the structural system, ie the inextensible cantilevered beam, have been studied in the literature [5,8,10] and are repeated here. Following the work of the authors, there are three equations of motion and three unknown variables: u is the displacement in the x direction, w in y, and λ is the Lagrange multiplier that enforces the inextensibility constraint. What follows is Eqn. 1 as the equation of motion for u, Eqn. 2 as the equation of motion for w, and Eqn. 3 as the constraint equation.

$$\ddot{\mathbf{u}} - \mathbf{A}\lambda = 0 \tag{1}$$

$$\ddot{\mathbf{w}} + 2\zeta \boldsymbol{\omega} \, \dot{\mathbf{w}} + \boldsymbol{\omega}^2 \, \mathbf{w} - \mathbf{B} \mathbf{w} \boldsymbol{\lambda} + \mathbf{P} \, \mathbf{w}^3 = 0 \tag{2}$$

$$\mathbf{u} + \frac{1}{2}\mathbf{A}^{-1}\mathbf{B}\mathbf{w}^2 = 0 \tag{3}$$

To add fluid forcing to this system, we adopt two forms of a pressure loading. The steady pressure differential across the plate will be due to oblique shock analysis at the clamped leading edge of the plate. The unsteady pressure distribution will be due to nonlinear piston theory, including a geometric modification to classical piston theory to ensure that the pressure is always acting normal to the surface of the plate.

The virtual work acting on the plate is given by

$$\delta W^{NC_{aero}} = \int_{0}^{L} b\Delta p \, \mathbf{n} \cdot \delta \mathbf{r} \, dx \tag{4}$$

where \mathbf{n} is the unit normal to the deflected plate and $\delta \mathbf{r}$ is the virtual displacement of the plate. Piston Theory is classically used to predict pressures only in the direction normal to the undeformed plate which intrinsically assumes that the slopes are small. The virtual work would then be expressed as Eqn. 5.

$$\delta W^{NC_{aero}} = \int_{0}^{L} b\Delta p \ \delta w \ dx \tag{5}$$

For fully pinned or clamped plates this assumption is valid. However, the small deflection assumption no longer holds for the case of a cantilevered plate, and therefore a large deflection expression must be derived.

2.1 Large Deflection Generalization of the Aerodynamic Model

Due to the large displacement of the beam, we understand that pressure must be everywhere normal to the deflected beam. Therefore, the pressure contributes to both the δu and δw components of the virtual work. To derive the correct form of the virtual work for this case, consider the beam with longitudinal deflection w in the \mathbf{i} direction and transverse deflection u in \mathbf{j} . The virtual displacement is $\delta \mathbf{r} = \delta u \mathbf{i} + \delta w \mathbf{j}$, and the local tangent vector to the deformed beam is $\mathbf{\tau} = \cos \beta \mathbf{i} + \sin \beta \mathbf{j}$, where β is the angle of the beam relative to the undeformed horizontal. Now the local normal to the deformed beam is $\mathbf{n} \equiv \mathbf{k} \times \boldsymbol{\tau} = -\sin \beta \mathbf{i} + \cos \beta \mathbf{j}$, and by incorporating this into Eqn. 4, the expression for virtual work is given by Eqn. 6.

$$\delta W^{NC_{aero}} = \int_{0}^{L} \left[-b\Delta p \sin(\beta) \, \delta u + b\Delta p \cos(\beta) \, \delta w \right] \, dx \tag{6}$$

Note that $\sin \beta$ and $\cos \beta$ are defined from geometric relationships as follows.

$$\tan \beta = \frac{\frac{\partial w}{\partial x}}{1 + \frac{\partial u}{\partial x}} = \frac{w_x}{1 + u_x} = \frac{w_x}{1 - 1/2w_x^2} \equiv f \tag{7}$$

$$\tan \beta = \frac{\sin \beta}{\cos \beta} = f \tag{8}$$

$$\sin^2 \beta + \cos^2 \beta = 1 \tag{9}$$

$$f^2 = \frac{\sin^2 \beta}{\cos^2 \beta} \tag{10}$$

So then,

$$(f^2+1)\cos^2\beta = 1\tag{11}$$

$$\cos \beta = \frac{1}{(f^2 + 1)^{1/2}} \tag{12}$$

From this, we can find $\sin \beta$ as well.

$$\sin \beta = \frac{f}{(f^2 + 1)^{1/2}} \tag{13}$$

Now, substituting 7 into 12 and 13, we can write the definitions of $\sin \beta$ and $\cos \beta$ in terms of w.

$$\cos \beta = (1 - w_x^2)^{1/2} \approx (1 - 1/2w_x^2) \tag{14}$$

$$\sin \beta = w_x \tag{15}$$

So, the expression for virtual work acting on the plate (Eqn. 6) can be written as follows.

$$\delta W^{NC_{aero}} = \int_{0}^{L} b\Delta p \left(-w_x \, \delta u + \left(1 - 1/2w_x^2 \right) \, \delta w \right) dx \tag{16}$$

2.2 Oblique Wave Theory

At the sharp, perfectly rigid corner at the leading edge of the panel, the flow is turned and oblique waves are generated. As shown in Fig. 1, on the side of the panel which is turned into the flow, there is a shock wave. On the side turned out of the flow, there is an expansion wave. This generates a pressure differential across the plate which causes a static deflection of the plate, as computed and shown in Fig. 2a. The pressures behind the clamped corner are computed with classical oblique shock theory and Prandtl-Meyer expansion fan theory, the formulations for which are omitted here but can be found in many references [12, 13]. Beyond this initial clamped corner, the plate is flexible and may produce other waves in a two-way coupling fashion between the fluid and the structure, and the pressures from these effects are calculated with piston theory.

To include the static pressure differential in the equations of motion, we substitute the pressure differential from the oblique wave analysis into Eqn. 16, and use the Rayleigh-Ritz method to separate variables into mode shapes and coefficients in both u and w. The mode shapes for u and w are the natural cantilever mode shapes and for λ the mode shapes are given by $\Psi_k^\lambda(x) = \sin\left(\frac{2k-1}{2\pi}(1-x)\right)$. For more details on the modal expansion of λ , see [10].

$$u = \sum_{i} \Psi_{i}^{u}(x)u_{i}(t) = \Psi_{\mathbf{u}}^{T}\mathbf{u}$$
(17)

$$w = \sum_{j} \Psi_{j}^{w}(x)w_{j}(t) = \Psi_{\mathbf{w}}^{T}\mathbf{w}$$
(18)

$$\lambda = \sum_{k} \Psi_{k}^{\lambda}(x) \lambda_{k}(t) = \Psi_{\lambda}^{T} \lambda$$
 (19)

$$\delta W^{NC_{aero}} = -\Delta p_0 \sum_{i} \sum_{j} \int_{0}^{L} \Psi_{j}^{w'} \Psi_{i}^{u} dx \ w_{j} \ \delta u_{i}$$

$$+ \Delta p_0 \sum_{j} \left(\int_{0}^{L} \Psi_{j}^{w} dx - \frac{1}{2} \sum_{j1} \sum_{j2} \int_{0}^{L} \Psi_{j1}^{w'} \Psi_{j2}^{w'} \Psi_{j}^{w} dx \ w_{j1} w_{j2} \right) \delta w_{j} \quad (20)$$

Note that the pressure is constant across the plate for this term and therefore Δp can be written outside of the integral. Nondimensionalizing and replacing the integrals with equivalent matrices, we have the following.

$$\delta \overline{W}^{NC_{aero}} = \frac{bL^3}{EI} \Delta p_0 \left(-\sum_i \sum_j Q_{ij}^{\Delta pu} \, \overline{w}_j \, \delta \overline{u}_i + \sum_j \left(Q_j^{\Delta pw1} - \frac{1}{2} \sum_{j1} \sum_{j2} Q_{jj1j2}^{\Delta pw2} \, \overline{w}_{j1} \overline{w}_{j2} \right) \delta \overline{w}_j \right)$$
(21)

Or, switching from index notation to a more compact matrix notation, where all bold Roman variables are vectors or matrices, we have the following.

$$\delta \overline{W}^{NC_{aero}} = \Delta \overline{p_0} \left(-\mathbf{Q}^{\Delta \mathbf{p} \mathbf{u}} \mathbf{w} \, \delta \mathbf{u} + \left(\mathbf{Q}^{\Delta \mathbf{p} \mathbf{w} \mathbf{1}} - \frac{1}{2} \, \mathbf{Q}^{\Delta \mathbf{p} \mathbf{w} \mathbf{2}} \, \mathbf{w} \mathbf{w} \right) \delta \mathbf{w} \right)$$
(22)

2.3 Piston Theory Aerodynamic Forcing

Piston theory [14–17] provides a simple relation between pressure perturbation and motion of a structure, one side of which is under a free stream flow with properties $\rho_{\infty}, U_{\infty}, M_{\infty}$. Because our plate model has fluid acting on both sides, and the fluid properites are not the same on both sides, we calculate a change in pressure across the upper and lower surfaces.

$$p_{upper} = \frac{\rho_u U_u}{M_l} \left[\left(\dot{w} + U_u \frac{\partial w}{\partial x} \right) + \frac{\gamma + 1}{4a_u} \left(\dot{w} + U_u \frac{\partial w}{\partial x} \right)^2 + \frac{\gamma + 1}{12a_u^2} \left(\dot{w} + U_u \frac{\partial w}{\partial x} \right)^3 \right]$$
(23)

$$p_{lower} = \frac{\rho_l U_l}{M_l} \left[\left(-\dot{w} - U_l \frac{\partial w}{\partial x} \right) + \frac{\gamma + 1}{4a_l} \left(-\dot{w} - U_l \frac{\partial w}{\partial x} \right)^2 + \frac{\gamma + 1}{12a_l^2} \left(-\dot{w} - U_l \frac{\partial w}{\partial x} \right)^3 \right] \tag{24}$$

Note that x is positive in the flow direction. Now we subtract the upper surface from the lower [16], and note the second order terms do not cancel one another since $U_u \neq U_l$.

$$\Delta p = p_{lower} - p_{upper} = -\left(\frac{\rho_l U_l}{M_l} + \frac{\rho_u U_u}{M_u}\right) \dot{w} - \left(\frac{\rho_l U_l^2}{M_l} + \frac{\rho_u U_u^2}{M_u}\right) \frac{\partial w}{\partial x}$$

$$+ \frac{\gamma + 1}{4} \left(\frac{\rho_l U_l}{M_l a_l} - \frac{\rho_u U_u}{M_u a_u}\right) \dot{w}^2 + \frac{\gamma + 1}{2} \left(\frac{\rho_l U_l^2}{M_l a_l} - \frac{\rho_u U_u^2}{M_u a_u}\right) \frac{\partial w}{\partial x} \dot{w} + \frac{\gamma + 1}{4} \left(\frac{\rho_l U_l^3}{M_l a_l} - \frac{\rho_u U_u^3}{M_u a_u}\right) \left(\frac{\partial w}{\partial x}\right)^2$$

$$- \frac{\gamma + 1}{12} \left(\frac{\rho_l U_l}{M_l a_l^2} + \frac{\rho_u U_u}{M_u a_u^2}\right) \dot{w}^3 - \frac{\gamma + 1}{4} \left(\frac{\rho_l U_l^2}{M_l a_l^2} + \frac{\rho_u U_u^2}{M_u a_u^2}\right) \frac{\partial w}{\partial x} \dot{w}^2 - \frac{\gamma + 1}{4} \left(\frac{\rho_l U_l^3}{M_l a_l^2} + \frac{\rho_u U_u^3}{M_u a_u^2}\right) \left(\frac{\partial w}{\partial x}\right)^2 \dot{w}$$

$$- \frac{\gamma + 1}{12} \left(\frac{\rho_l U_l^4}{M_l a_l^2} + \frac{\rho_u U_u^4}{M_u a_u^2}\right) \left(\frac{\partial w}{\partial x}\right)^3 \quad (25)$$

2.4 Dimensionless Parameters

When nondimensionalizing length, the following relationships are important.

$$x = L\xi$$
 $\frac{\partial}{\partial x} = \frac{1}{L} \frac{\partial}{\partial \xi}$ $\frac{\partial^2}{\partial x^2} = \frac{1}{L^2} \frac{\partial^2}{\partial \xi^2}$ (26)

We can also nondimensionalize time and its derivatives as follows, where the overlined terms are dimensionless.

$$t = \left(\frac{mL^4}{EI}\right)^{1/2} \bar{t} \qquad \frac{\partial}{\partial t} = \left(\frac{EI}{mL^4}\right)^{1/2} \frac{\partial}{\partial \bar{t}} \qquad \frac{\partial^2}{\partial t^2} = \frac{EI}{mL^4} \frac{\partial^2}{\partial \bar{t}^2}$$
(27)

In addition, we can use the following nondimensional parameters to describe the fluid and structural parameters. Note that μ is the aerodynamic to structural mass ratio and Λ is the aerodynamic to structural compliance ratio and both incorporate the Mach number in their definition.

$$\mu \equiv \frac{\rho_{\infty}bL}{mM_{\infty}} \tag{28}$$

$$\Lambda \equiv \frac{\rho_{\infty} U_{\infty}^2 b L^3}{EIM_{\infty}} \tag{29}$$

$$(\Lambda \mu)^{1/2} = \frac{\rho_{\infty} U_{\infty} b L^2}{M_{\infty} (EIm)^{1/2}}$$
 (30)

2.5 Simplifying Equation 25

Because the top and bottom freestream flow parameters are not equal, Eqn. 25 is much more cumbersome than classic third order piston theory expression when the top and bottom flow is the same. We can clean this up by a clever use of matrix algebra. First, note that

$$\left(\frac{\rho_l U_l}{M_l} + \frac{\rho_u U_u}{M_u}\right) = \underbrace{\begin{bmatrix} \rho_l U_l & \rho_u U_u \\ M_l & M_u \end{bmatrix}}_{\hat{\mathbf{q}}^T} \begin{Bmatrix} 1 \\ 1 \end{Bmatrix}$$
(31)

Defining the coefficient matrix as $\hat{\mathbf{q}}^T$ to denote that it represents a type of dynamic pressure, we can rewrite Eqn. 25 with this new notation.

$$\Delta p = \underline{\hat{\mathbf{q}}}^T \left(-\left(\left\{ \frac{1}{1} \right\} \dot{w} + \left\{ \frac{U_l}{U_u} \right\} w_x \right) + \frac{\gamma + 1}{4} \left(\left\{ \frac{a_l^{-1}}{-a_u^{-1}} \right\} \dot{w}^2 + 2 \left\{ \frac{U_l a_l^{-1}}{-U_u a_u^{-1}} \right\} w_x \dot{w} + \left\{ \frac{U_l^2 a_l^{-1}}{-U_u^2 a_u^{-1}} \right\} w_x^2 \right) \\ - \frac{\gamma + 1}{12} \left(\left\{ \frac{a_l^{-2}}{a_u^{-2}} \right\} \dot{w}^3 + 3 \left\{ \frac{U_l a_l^{-2}}{U_u a_u^{-2}} \right\} w_x \dot{w}^2 + 3 \left\{ \frac{U_l^2 a_l^{-2}}{U_u^2 a_u^{-2}} \right\} w_x^2 \dot{w} + \left\{ \frac{U_l^3 a_l^{-2}}{U_u^3 a_u^{-2}} \right\} w_x^3 \right) \right)$$
(32)

Let's nondimensionalize $\underline{\hat{\mathbf{q}}}^T$ by multiplying and dividing by the freestream parameters upstream of the control surface.

$$\underline{\hat{\mathbf{q}}}^{T} = \begin{bmatrix} \frac{\rho_{l}U_{l}}{M_{l}} & \frac{\rho_{u}U_{u}}{M_{u}} \end{bmatrix} \begin{pmatrix} \frac{M_{\infty}}{\rho_{\infty}U_{\infty}} \end{pmatrix} \begin{pmatrix} \frac{\rho_{\infty}U_{\infty}}{M_{\infty}} \end{pmatrix} = \begin{bmatrix} \frac{\rho_{l}U_{l}M_{\infty}}{M_{l}\rho_{\infty}U_{\infty}} & \frac{\rho_{u}U_{u}M_{\infty}}{M_{u}\rho_{\infty}U_{\infty}} \end{bmatrix} \begin{pmatrix} \frac{\rho_{\infty}U_{\infty}}{M_{\infty}} \end{pmatrix} \equiv \underline{\mathbf{q}}^{T} \begin{pmatrix} \frac{\rho_{\infty}U_{\infty}}{M_{\infty}} \end{pmatrix}$$
(33)

$$\underline{\mathbf{q}}^T \equiv \begin{bmatrix} \frac{\rho_l U_l M_{\infty}}{M_l \rho_{\infty} U_{\infty}} & \frac{\rho_u U_u M_{\infty}}{M_u \rho_{\infty} U_{\infty}} \end{bmatrix}$$
(34)

Note that q^T without the hat is dimensionless.

Finally in each vector with U_i or a_i , we will multiply and divide by the freestream flow velocity U_{∞} or speed of sound a_{∞} , such that $\overline{U_i} = U_i/U_{\infty}$ and $\overline{a_i} = a_i/a_{\infty}$ For example,

2.6 First Order Piston Theory

For first order piston theory, we neglect the third order term in Eqn. 32, so the change in pressure across the beam is as follows.

$$\Delta p = -\underline{\hat{\mathbf{q}}}^T \left(\begin{cases} 1\\1 \end{cases} \dot{w} + \begin{cases} U_l\\U_u \end{cases} \frac{\partial w}{\partial x} \right) \tag{36}$$

Note the difference between Eqn. 36 and the expression for classical first order piston theory, $\Delta p = -2\frac{\rho_{\infty}U_{\infty}}{M_{\infty}}(\dot{w} + U_{\infty}w_x)$.

Nondimensionalizing the dynamic pressure and the terms inside the parentheses, we get the following.

$$\Delta p = -\left(\frac{\rho_{\infty}U_{\infty}}{M_{\infty}}\right)\underline{\mathbf{q}}^{T}\left(L\left(\frac{EI}{mL^{4}}\right)^{1/2} \begin{Bmatrix} 1\\1 \end{Bmatrix} \overline{\dot{w}} + \begin{Bmatrix} \overline{U_{l}}\\\overline{U_{u}} \end{Bmatrix} U_{\infty}\frac{\partial \overline{w}}{\partial \xi}\right)$$
(37)

Now insert Eqn. 37 into Eqn. 16 to get the virtual work done by first order piston theory. Note that we've already pulled out a factor of L^2 to account for the virtual displacments and the integration across the length.

$$\delta W^{NC_{aero}} = -\int_{0}^{1} L^{2}b \left(\frac{\rho_{\infty}U_{\infty}}{M_{\infty}}\right) \mathbf{q}^{T} \left(L\left(\frac{EI}{mL^{4}}\right)^{1/2} \begin{Bmatrix} 1\\1 \end{Bmatrix} \overline{w} + \begin{Bmatrix} \overline{U_{l}}\\\overline{U_{u}} \end{Bmatrix} U_{\infty} \frac{\partial \overline{w}}{\partial \xi} \right) \times \left(-\overline{w_{x}} \delta \overline{u} + (1 - 1/2\overline{w_{x}}^{2}) \delta \overline{w}\right) d\xi \quad (38)$$

Now if we divide both sides by EI/L to nondimensionalize work, we get the following.

$$\frac{L}{EI}\delta W^{NC_{aero}} \equiv \delta \overline{W}^{NC_{aero}} = -\int_{0}^{1} \underline{\mathbf{q}}^{T} \left(\left(\frac{\rho_{\infty} U_{\infty} bL^{2}}{M_{\infty} (EIm)^{1/2}} \right) \begin{Bmatrix} 1 \\ 1 \end{Bmatrix} \overline{w} + \left(\frac{\rho_{\infty} U_{\infty}^{2} bL^{3}}{EIM_{\infty}} \right) \begin{Bmatrix} \overline{U_{l}} \\ \overline{U_{u}} \end{Bmatrix} \frac{\partial \overline{w}}{\partial \xi} \right) \times \left(-\overline{w_{x}} \delta \overline{u} + (1 - 1/2\overline{w_{x}}^{2}) \delta \overline{w} \right) d\xi \quad (39)$$

And finally we arrive at the expression for first order piston theory, using the dimensionless parameters Λ and μ .

$$\delta \overline{W}^{NC_{aero}} = -\int_{0}^{1} \mathbf{q}^{T} \left((\Lambda \mu)^{1/2} \begin{Bmatrix} 1 \\ 1 \end{Bmatrix} \overline{\dot{w}} + \Lambda \begin{Bmatrix} \overline{U_{l}} \\ \overline{U_{u}} \end{Bmatrix} \frac{\partial \overline{w}}{\partial \xi} \right) \left(-\overline{w_{x}} \, \delta \overline{u} + (1 - 1/2 \overline{w_{x}}^{2}) \, \delta \overline{w} \right) d\xi$$

$$(40)$$

2.7 Second and Third Order Piston Theory

We can extend the previous analysis to derive the virtual work from second and third order piston theory. Note that we will use delta functions to include or exclude the second and third order terms. For example, if we are evaluating a second order case, we set $\delta_2=1$ and $\delta_3=0$, and for a third order case, $\delta_2=\delta_3=1$.

$$\delta \overline{W}^{NC_{aero}} = -\int_{0}^{1} \underline{\mathbf{q}}^{T} \left((\Lambda \mu)^{1/2} \begin{Bmatrix} 1 \\ 1 \end{Bmatrix} \overline{w} + \Lambda \begin{Bmatrix} \overline{U_{l}} \\ \overline{U_{u}} \end{Bmatrix} \overline{w_{x}}
+ \delta_{2} \frac{M_{\infty}(\gamma + 1)}{4} \left(\mu \begin{Bmatrix} \overline{a_{l}}^{-1} \\ -\overline{a_{u}}^{-1} \end{Bmatrix} \overline{w}^{2} + 2(\Lambda \mu)^{1/2} \begin{Bmatrix} \overline{U_{l}} \overline{a_{l}}^{-1} \\ -\overline{U_{u}} \overline{a_{u}}^{-1} \end{Bmatrix} \overline{w_{x}} \overline{w} + \Lambda \begin{Bmatrix} \overline{U_{l}}^{2} \overline{a_{l}}^{-1} \\ -\overline{U_{u}}^{2} \overline{a_{l}}^{-1} \end{Bmatrix} \overline{w_{x}}^{2} \right)
+ \delta_{3} \frac{M_{\infty}^{2}(\gamma + 1)}{12} \left(\left(\frac{\mu^{3}}{\Lambda} \right)^{1/2} \begin{Bmatrix} \overline{a_{l}}^{-2} \\ \overline{a_{u}}^{-2} \end{Bmatrix} \overline{w}^{3} + 3\mu \begin{Bmatrix} \overline{U_{l}} \overline{a_{l}}^{-2} \\ \overline{U_{l}} \overline{a_{u}}^{-2} \end{Bmatrix} \overline{w_{x}} \overline{w}^{2} \right)
+ 3(\Lambda \mu)^{1/2} \begin{Bmatrix} \overline{U_{l}}^{2} \overline{a_{l}}^{-2} \\ \overline{U_{u}}^{2} \overline{a_{l}}^{-2} \end{Bmatrix} \overline{w_{x}}^{2} \overline{w} + \Lambda \begin{Bmatrix} \overline{U_{l}}^{3} \overline{a_{l}}^{-2} \\ \overline{U_{u}}^{3} \overline{a_{u}}^{-2} \end{Bmatrix} \overline{w_{x}}^{3} \right) \right)
\times \left(-\overline{w_{x}} \delta \overline{u} + (1 - 1/2\overline{w_{x}}^{2}) \delta \overline{w} \right) d\xi \quad (41)$$

2.8 First Order Scaling Analysis

In previous work [5], we utilized a scaling analysis to justify neglecting some higher order terms. Here we employ the same idea. Scale \overline{w} by $\omega \overline{w}$. The order of each term is as follows, based upon dimensional quantities given in the appendix.

$$\mu = O[10^{-2}]$$

$$\Lambda = O[10^{2}]$$

$$\overline{\omega} = O[10^{2}]$$

$$\overline{w} = O[10^{-1}]$$

$$\frac{\partial \overline{w}}{\partial \xi} = O[10^{-1}]$$

$$\delta \overline{W}^{NC_{aero}} = -\int_{0}^{1} \underline{\mathbf{q}}^{T} \left((\Lambda \mu)^{1/2} \begin{Bmatrix} 1 \\ 1 \end{Bmatrix} \overline{\dot{w}} + \Lambda \begin{Bmatrix} \overline{U_{l}} \\ \overline{U_{u}} \end{Bmatrix} \frac{\partial \overline{w}}{\partial \xi} \right) \left(-\overline{w_{x}} \, \delta \overline{u} + (1 - 1/2\overline{w_{x}}^{2}) \, \delta \overline{w} \right) d\xi$$
(42)

$$\delta \overline{W}^{NC_{aero}} = \int_{0}^{1} \underline{\mathbf{q}}^{T} \left(\delta_{\beta} \left((\Lambda \mu)^{1/2} \begin{Bmatrix} 1 \\ 1 \end{Bmatrix} \overline{w_{x}} \overline{w} + \Lambda \begin{Bmatrix} \overline{U_{l}} \\ \overline{U_{u}} \end{Bmatrix} \overline{w_{x}}^{2} \right) \delta \overline{u}
+ \left(- (\Lambda \mu)^{1/2} \begin{Bmatrix} 1 \\ 1 \end{Bmatrix} \overline{w} + 1/2 \delta_{\beta} (\Lambda \mu)^{1/2} \begin{Bmatrix} 1 \\ 1 \end{Bmatrix} \overline{w_{x}}^{2} \overline{w} - \Lambda \begin{Bmatrix} \overline{U_{l}} \\ \overline{U_{u}} \end{Bmatrix} \overline{w_{x}} + 1/2 \delta_{\beta} \Lambda \begin{Bmatrix} \overline{U_{l}} \\ \overline{U_{u}} \end{Bmatrix} \overline{w_{x}}^{3} \right) \delta \overline{w} \right) d\xi$$
(43)

Assuming that $\overline{U_l}$ and $\overline{U_u}$ are order 1, this leads to the following order of each term.

$$(O[10^{0}] + O[10^{1}]) \delta \overline{u} + (O[10^{1}] + O[10^{-1}] + O[10^{1}] + O[10^{-1}]) \delta \overline{w}$$
(44)

Note that the nonlinear terms which contribute to the virtual work in u via of the β effect are marked with a delta function where these terms can be included or excluded by setting δ_{β} equal to zero or one. Note also that these terms are of the same order than some linear terms in w, illuminating the importance of the β effect. For the first order approximation, we keep all terms. Moving forward, we will discard any terms of order $O[10^{-2}]$ or higher.

2.9 Second and Third Order Scaling Analysis

Utilizing the same method outlined above, we can simplify the second and third order piston theory expressions greatly. It can be shown that the virtual work due to piston theory aerodynamics may be simplified to the following.

$$\delta \overline{W}^{NC_{aero}} = \int_{0}^{1} \mathbf{q}^{T} \left(\delta_{\beta} \left((\Lambda \mu)^{1/2} \begin{Bmatrix} 1 \\ 1 \end{Bmatrix} \overline{w_{x}} \overline{w} + \Lambda \begin{Bmatrix} \overline{U_{l}} \\ \overline{U_{u}} \end{Bmatrix} \overline{w_{x}}^{2} \right) \delta \overline{u}
+ \left(- (\Lambda \mu)^{1/2} \begin{Bmatrix} 1 \\ 1 \end{Bmatrix} \overline{w} + 1/2 \delta_{\beta} (\Lambda \mu)^{1/2} \begin{Bmatrix} 1 \\ 1 \end{Bmatrix} \overline{w_{x}}^{2} \overline{w} - \Lambda \begin{Bmatrix} \overline{U_{l}} \\ \overline{U_{u}} \end{Bmatrix} \overline{w_{x}} + 1/2 \delta_{\beta} \Lambda \begin{Bmatrix} \overline{U_{l}} \\ \overline{U_{u}} \end{Bmatrix} \overline{w_{x}}^{3}
+ \delta_{2} \frac{M_{\infty} (\gamma + 1)}{4} \left(\mu \begin{Bmatrix} \overline{a_{l}}^{-1} \\ -\overline{a_{u}}^{-1} \end{Bmatrix} \overline{w}^{2} + 2(\Lambda \mu)^{1/2} \begin{Bmatrix} \overline{U_{l}} \overline{a_{l}}^{-1} \\ -\overline{U_{u}} \overline{a_{u}}^{-1} \end{Bmatrix} \overline{w_{x}} \overline{w} + \Lambda \begin{Bmatrix} \overline{U_{l}}^{2} \overline{a_{l}}^{-1} \\ -\overline{U_{u}}^{2} \overline{a_{u}}^{-1} \end{Bmatrix} \overline{w_{x}}^{2} \right)
+ \delta_{3} \frac{M_{\infty}^{2} (\gamma + 1)}{12} \left(\left(\frac{\mu^{3}}{\Lambda} \right)^{1/2} \begin{Bmatrix} \overline{a_{l}}^{-2} \\ \overline{a_{u}}^{-2} \end{Bmatrix} \overline{w}^{3} + 3\mu \begin{Bmatrix} \overline{U_{l}} \overline{a_{l}}^{-2} \\ \overline{U_{u}} \overline{a_{u}}^{-2} \end{Bmatrix} \overline{w_{x}} \overline{w}^{2}
+ 3(\Lambda \mu)^{1/2} \begin{Bmatrix} \overline{U_{l}}^{2} \overline{a_{l}}^{-2} \\ \overline{U_{u}}^{2} \overline{a_{u}}^{-2} \end{Bmatrix} \overline{w_{x}}^{2} \overline{w} + \Lambda \begin{Bmatrix} \overline{U_{l}}^{3} \overline{a_{l}}^{-2} \\ \overline{U_{u}}^{3} \overline{a_{u}}^{-2} \end{Bmatrix} \overline{w_{x}}^{3} \right) \delta \overline{w} \right) d\xi \quad (45)$$

Using the Rayleigh-Ritz approximation of this equation, we have the following.

Switching to matrix notation in which each Q represents a multidimensional matrix of integrated mode shapes, and each w is a vector of w modal coefficients, we can simplify the ex-

pression.

$$\delta \overline{W}^{NC_{aero}} = \underline{\mathbf{q}}^{T} \delta_{\beta} \left((\Lambda \mu)^{1/2} \begin{Bmatrix} 1 \\ 1 \end{Bmatrix} \mathbf{Q}_{1} \mathbf{w} \dot{\mathbf{w}} + \Lambda \begin{Bmatrix} \overline{U_{l}} \\ \overline{U_{u}} \end{Bmatrix} \mathbf{Q}_{2} \mathbf{w}^{2} \right) \delta \mathbf{u}
+ \underline{\mathbf{q}}^{T} \left(-(\Lambda \mu)^{1/2} \begin{Bmatrix} 1 \\ 1 \end{Bmatrix} \mathbf{Q}_{3} \mathbf{w} - \Lambda \begin{Bmatrix} \overline{U_{l}} \\ \overline{U_{u}} \end{Bmatrix} \mathbf{Q}_{4} \mathbf{w} + 1/2 \delta_{\beta} (\Lambda \mu)^{1/2} \begin{Bmatrix} 1 \\ 1 \end{Bmatrix} \mathbf{Q}_{5} \mathbf{w}^{2} \dot{\mathbf{w}} + 1/2 \delta_{\beta} \Lambda \begin{Bmatrix} \overline{U_{l}} \\ \overline{U_{l}} \end{Bmatrix} \mathbf{Q}_{6} \mathbf{w}^{3}
+ \delta_{2} \frac{M_{\infty}(\gamma + 1)}{4} \left(\mu \begin{Bmatrix} \overline{a_{l}}^{-1} \\ -\overline{a_{u}}^{-1} \end{Bmatrix} \mathbf{Q}_{7} \dot{\mathbf{w}}^{2} + 2(\Lambda \mu)^{1/2} \begin{Bmatrix} \overline{U_{l}} \overline{a_{l}}^{-1} \\ -\overline{U_{u}} \overline{a_{u}}^{-1} \end{Bmatrix} \mathbf{Q}_{8} \mathbf{w} \dot{\mathbf{w}} + \Lambda \begin{Bmatrix} \overline{U_{l}}^{2} \overline{a_{l}}^{-1} \\ -\overline{U_{u}}^{2} \overline{a_{u}}^{-1} \end{Bmatrix} \mathbf{Q}_{9} \mathbf{w}^{2} \right)
+ \delta_{3} \frac{M_{\infty}^{2} (\gamma + 1)}{12} \left(\left(\frac{\mu^{3}}{\Lambda} \right)^{1/2} \begin{Bmatrix} \overline{a_{l}}^{-2} \\ \overline{a_{u}}^{-2} \end{Bmatrix} \mathbf{Q}_{10} \dot{\mathbf{w}}^{3} + 3\mu \begin{Bmatrix} \overline{U_{l}} \overline{a_{l}}^{-2} \\ \overline{U_{u}} \overline{a_{u}}^{-2} \end{Bmatrix} \mathbf{Q}_{11} \mathbf{w} \dot{\mathbf{w}}^{2}
+ 3(\Lambda \mu)^{1/2} \begin{Bmatrix} \overline{U_{l}}^{2} \overline{a_{l}}^{-2} \\ \overline{U_{u}}^{2} \overline{a_{u}}^{-2} \end{Bmatrix} \mathbf{Q}_{5} \mathbf{w}^{2} \dot{\mathbf{w}} + \Lambda \begin{Bmatrix} \overline{U_{l}}^{3} \overline{a_{l}}^{-2} \\ \overline{U_{u}}^{3} \overline{a_{u}}^{-2} \end{Bmatrix} \mathbf{Q}_{6} \mathbf{w}^{3} \right) \delta \mathbf{w} \quad (47)$$

Now we can separate this into components according to $\delta \mathbf{u}$ or $\delta \mathbf{w}$,

$$\mathbf{Q}^{PT_u} = \underline{\mathbf{q}}^T \delta_{\beta} \left(\left(\Lambda \mu \right)^{1/2} \begin{Bmatrix} 1 \\ 1 \end{Bmatrix} \mathbf{Q_1} \mathbf{w} \dot{\mathbf{w}} + \Lambda \begin{Bmatrix} \overline{U_l} \\ \overline{U_u} \end{Bmatrix} \mathbf{Q_2} \mathbf{w}^2 \right)$$
(48)

$$\mathbf{Q}^{PT_{w}} = \underline{\mathbf{q}}^{T} \left(-(\Lambda \mu)^{1/2} \begin{Bmatrix} 1 \\ 1 \end{Bmatrix} \mathbf{Q_{3}w} - \Lambda \begin{Bmatrix} \overline{U_{l}} \\ \overline{U_{u}} \end{Bmatrix} \mathbf{Q_{4}w} + 1/2\delta_{\beta} \left(\Lambda \mu \right)^{1/2} \begin{Bmatrix} 1 \\ 1 \end{Bmatrix} \mathbf{Q_{5}w^{2}\dot{\mathbf{w}}} + 1/2\delta_{\beta} \Lambda \begin{Bmatrix} \overline{U_{l}} \\ \overline{U_{u}} \end{Bmatrix} \mathbf{Q_{6}w^{3}} \right)$$

$$+ \delta_{2} \frac{M_{\infty}(\gamma + 1)}{4} \left(\mu \begin{Bmatrix} \overline{a_{l}}^{-1} \\ -\overline{a_{u}}^{-1} \end{Bmatrix} \mathbf{Q_{7}\dot{\mathbf{w}}}^{2} + 2(\Lambda \mu)^{1/2} \begin{Bmatrix} \overline{U_{l}}\overline{a_{l}}^{-1} \\ -\overline{U_{u}}\overline{a_{u}}^{-1} \end{Bmatrix} \mathbf{Q_{8}w\dot{\mathbf{w}}} + \Lambda \begin{Bmatrix} \overline{U_{l}^{2}}\overline{a_{l}}^{-1} \\ -\overline{U_{u}^{2}}\overline{a_{u}}^{-1} \end{Bmatrix} \mathbf{Q_{9}w^{2}} \right)$$

$$+ \delta_{3} \frac{M_{\infty}^{2}(\gamma + 1)}{12} \left(\left(\frac{\mu^{3}}{\Lambda} \right)^{1/2} \begin{Bmatrix} \overline{a_{l}}^{-2} \\ \overline{a_{u}}^{-2} \end{Bmatrix} \mathbf{Q_{10}\dot{\mathbf{w}}}^{3} + 3\mu \begin{Bmatrix} \overline{U_{l}}\overline{a_{l}}^{-2} \\ \overline{U_{u}}\overline{a_{u}}^{-2} \end{Bmatrix} \mathbf{Q_{11}w\dot{\mathbf{w}}}^{2}$$

$$+ 3(\Lambda \mu)^{1/2} \begin{Bmatrix} \overline{U_{l}^{2}}\overline{a_{l}}^{-2} \\ \overline{U_{u}^{2}}\overline{a_{u}}^{-2} \end{Bmatrix} \mathbf{Q_{5}w^{2}\dot{\mathbf{w}}} + \Lambda \begin{Bmatrix} \overline{U_{l}^{3}}\overline{a_{l}}^{-2} \\ \overline{U_{u}^{3}}\overline{a_{u}}^{-2} \end{Bmatrix} \mathbf{Q_{6}w^{3}} \right)$$

$$(49)$$

and finally we arrive at the equations of motion. Note that the $\Delta \overline{p_0}$ terms represent the steady pressure differential due to the leading edge shock and the \mathbf{Q}^{PT} terms are the unsteady piston theory terms.

$$\ddot{\mathbf{u}} - \mathbf{A}\boldsymbol{\lambda} = -\Delta \overline{p_0} \mathbf{Q}^{\Delta p \mathbf{u}} \mathbf{w} + \mathbf{Q}^{PT_u}$$

$$\ddot{\mathbf{w}} + 2\boldsymbol{\zeta}\boldsymbol{\omega} \dot{\mathbf{w}} + \boldsymbol{\omega}^2 \mathbf{w} - \mathbf{B}\mathbf{w}\boldsymbol{\lambda} + \mathbf{P} \mathbf{w}^3 = \Delta \overline{p_0} \left(\mathbf{Q}^{\Delta p \mathbf{w} \mathbf{1}} - \frac{1}{2} \mathbf{Q}^{\Delta p \mathbf{w} \mathbf{2}} \mathbf{w} \mathbf{w} \right) + \mathbf{Q}^{PT_w}$$

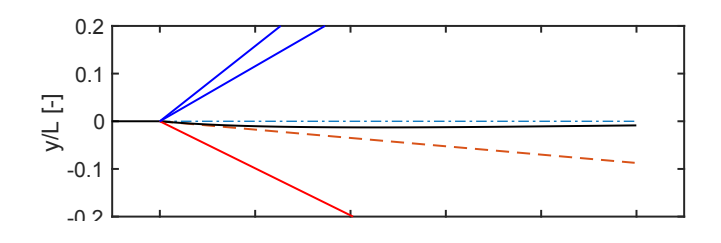
$$\mathbf{u} + \frac{1}{2} \mathbf{A}^{-1} \mathbf{B} \mathbf{w}^2 = 0$$

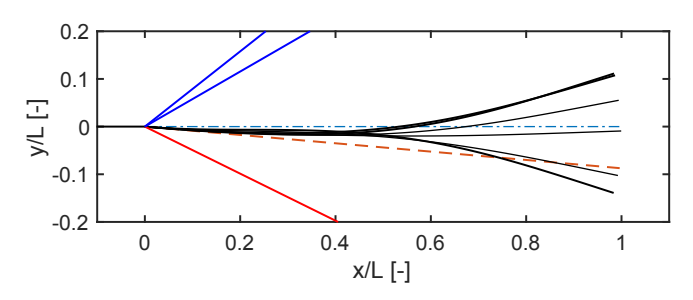
$$(50)$$

These equations are manipulated into one equation for w and then solved in time using Matlab's fourth order Runge-Kutta solver, ode 45.

3 RESULTS

We are interested in the dynamic behavior of the plate at and around the flutter point, ie the critical value of the nondimensional flow dynamic pressure Λ where the plate behavior changes from a static deflection to a limit cycle oscillation (LCO). Figure 2 illustrates a canonical case for each response type with a Mach 2 flow over a 5°corner angle. The surface's static deflection with a Λ value of 60 and μ value of 0.0241 is shown in Fig. 2a, while the LCO of the surface





(b) Samples of LCO deflections over one period, supercritical $\Lambda=72$

Figure 2: Steady state and LCO deflections of control surface with incidence angle of 5°, Mach 2. Black lines show control surface, blue lines are the expansion fan, red line is the oblique shock, dot-dash cyan line is the horizontal, and dashed orange shows the incidence angle

with a Λ value of 72 and μ value of 0.0256 is shown in Fig. 2b. In each figure, the black lines represent the structure itself, the two blue lines above the structure are the Mach lines which make up the front and rear of the expansion fan, the red line below the plot is the weak oblique shock wave. The dashed orange line shows the corner angle while the light blue dash-dotted line shows the undeformed horizontal. From Fig. 2a, we can visualize how the pressure differential across the plate from the corner angle shock behavior influences the plate's static deflection. From Fig. 2b, we can expect that the LCO is primarily a combination of the first and second natural bending modes.

The results herein depict several types of sensitivity. One is the sensitivity to numerical methods such as the number of modes used. Another is the sensitivity to the mathematical model of the physical system. Finally, the third is the sensitivity to the parameters within the model. To illustrate the sensitivity to the numerical methods, a modal convergence study was performed, and the results are shown in Fig. 3. For these cases, the number of modes in each component was set to either 2, 4, or 6. It can be seen that the cases with 4 and 6 modes are nearly identical until the deflection grows above 15% of the plate length, and therefore 4 modes are deemed to be sufficient for these computations.

These equations of motion are attractive due to their transparency into the system. By including or omitting the nonlinear terms in the equations, one may examine the sensitivity the system has to the mathematical model which describes it. The behavior of the beam with and without these nonlinearities has been studied previously [10], and this work again shows that the nonlinear inertia dominates the nonlinear stiffness due to geometric nonlinearities, as seen in Fig. 4. Because flutter is a linear phenomenon, the flutter point does not change as we change the nonlinear parameters of the model, however the LCO behavior changes dramatically. Compared to the solution with a linear structure, the solution is similar when stiffness nonlinearities are incorporated. By including inertia nonlinearities, the LCO amplitude nearly doubles. When

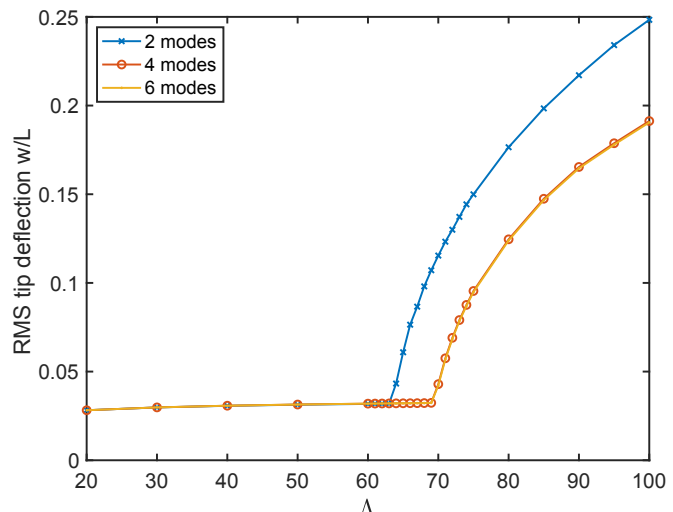


Figure 3: Modal convergence of Mach 2 flow over a 2° corner angle. Number of modes is equal among all components u, w, and Λ .

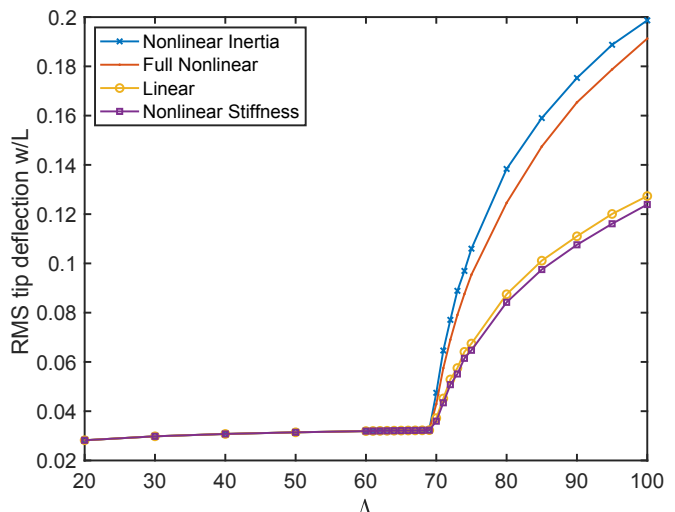


Figure 4: Influence of structural nonlinearities on LCO amplitude

both are included, the nonlinear stiffness somewhat lowers the LCO amplitude, but the system is still clearly dominated by the nonlinear inertia.

Similarly, we can explore the effects of including or omitting the aerodynamic nonlinearities in the form of the piston theory expansion terms. Figure 5 shows the effect for two cases of corner angle θ . In both cases, the third order piston theory predicts higher LCO amplitude. However, it is clear that the inclusion of second order terms has a smaller effect than the third order terms. This is because the pressure from the upper and lower surfaces are subtractive rather than additive in the second order terms, and at these conditions the pressures are nearly identical. To illustrate this effect, the second order effects in Fig. 5a where $\theta=2^{\circ}$ are nearly zero but they are non-negligible in the case of Fig. 5b where $\theta=5^{\circ}$. Because in the higher corner angle case, the pressure acting on the top and bottom surfaces differ more than in the smaller corner angle case, the second order effect is greater. Indeed, in the case where $\theta=0^{\circ}$, the second order terms sum to zero by definition.

Finally we arrive at the sensitivity to the model parameters themselves. In Figs. 6 and 7, the influences of the freestream Mach number and the corner angle θ are respectively explored. Note

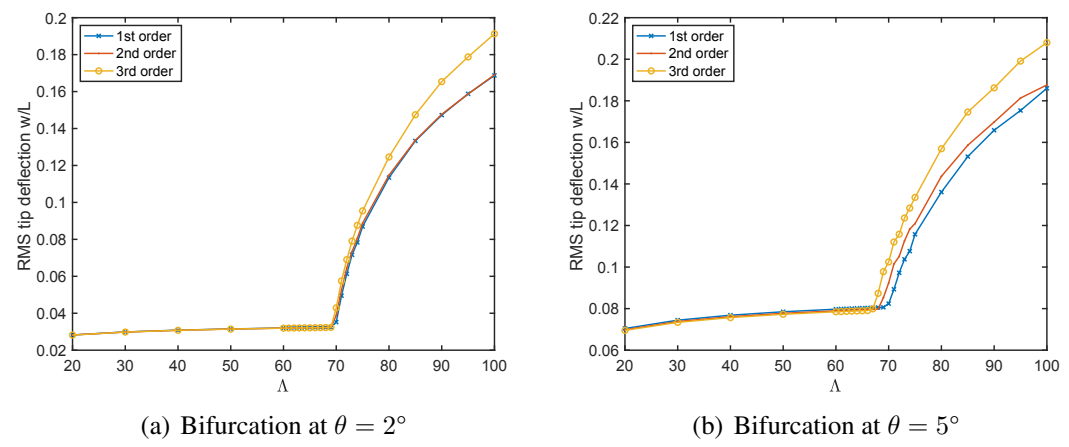


Figure 5: Sensitivities of the model to different orders of Piston Theory, for an initial corner angle of (a) $\theta=2^{\circ}$ and (b) $\theta=5^{\circ}$.

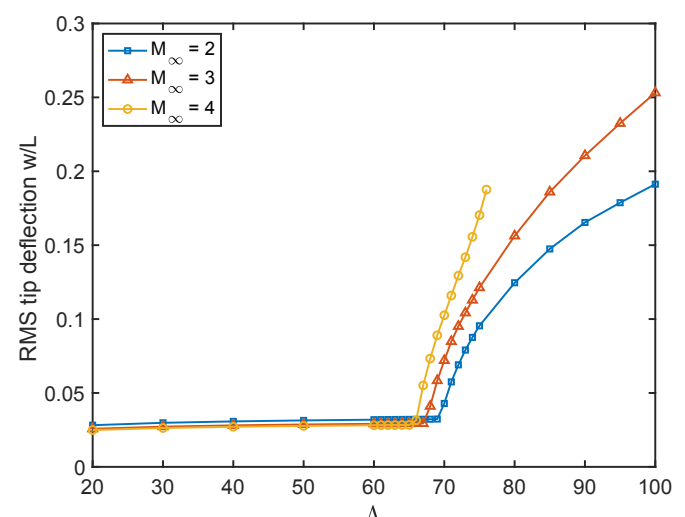


Figure 6: Influence of Mach number on static deflection, flutter point, and LCO amplitude. Note that where the Mach 4 solutions are not plotted is where the solutions diverge to infinity.

that for first order piston theory, the Mach number only appears embedded within the parameters Λ and μ , but for second and third order piston theory, the Mach number appears on its own. Therefore, for nonlinear flow theory, the model may be sensitive to the Mach number. Figure 6 shows this sensitivity. Note that the higher Mach number flow has a slightly lower flutter point than lower Mach numbers due to the difference in static pressure differential. More importantly though, the LCO amplitudes are higher at higher Mach numbers. Note, interestingly, that the Mach 4 flow plot abruptly ends just before $\Lambda=80$. Beyond this Λ level, the solution oscillates toward \pm infinity, ie it is no longer a stable limit cycle. This has been documented by the authors previously, and it was found that each Mach number has a point at which the solutions tend toward the infinities, and that these points are coincident with a specific RMS tip deflection level times the Mach number. This aligns with classical literature [14] which states that there is some high speed similitude parameter beyond which piston theory is invalid.

Figure 7 is interesting in that it shows clearly the effect of the initial corner angle on the system as well as the flow parameters. With no angle, the subcritical Λ values produce no static deflection of the plate, since both sides of the plate experiences the same pressure. A bifurcation to a LCO then occurs and the plate oscillates about the static equilibrium of zero. As the corner angle increases, the static deflection increases, owing to the pressure differential on either side

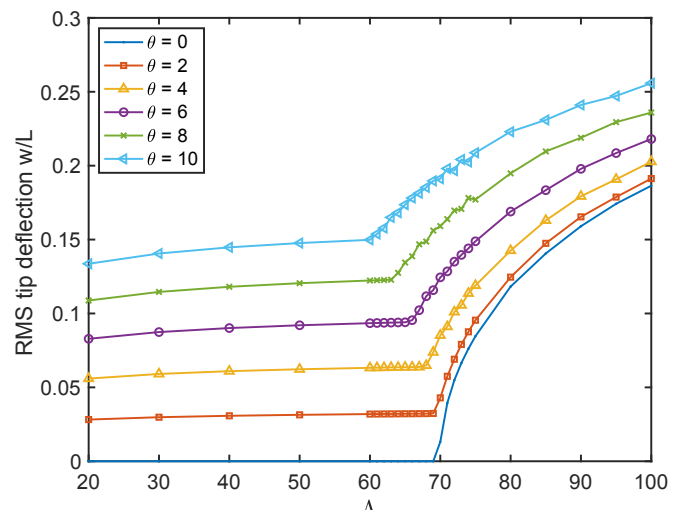


Figure 7: Influence of corner angle θ on static deflection, flutter point, and LCO amplitude

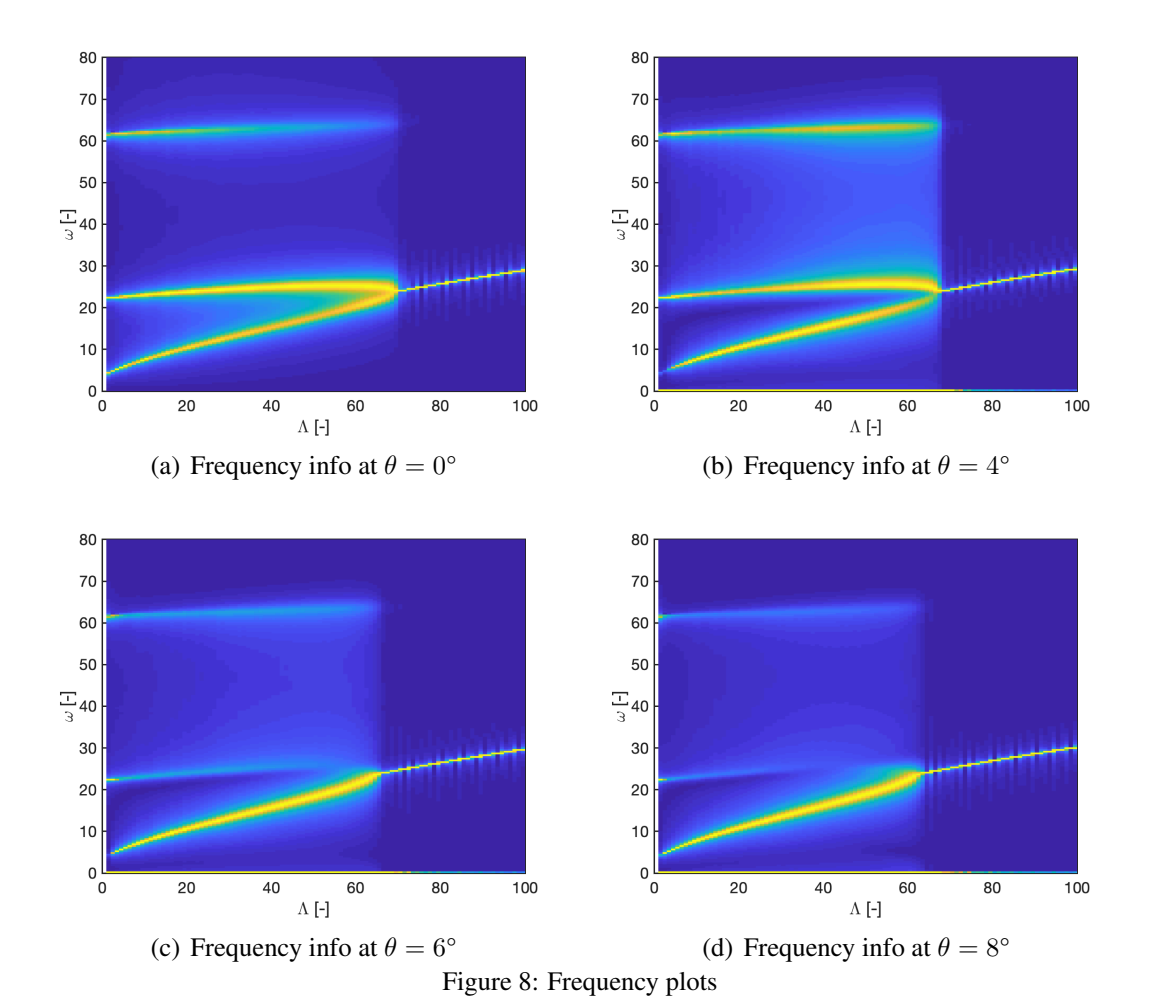
of the plate. Once a bifurcation occurs, the LCO amplitude is higher than the zero angle case because the plate is oscillating about a nonzero equilibrium. It is interesting to note, however that the flutter point occurs at lower Λ values for higher θ values, indicating that the stability of the system is affected by the pressure differential across the plate.

Because θ influences the static deflection of the plate, it is natural to ask if this influences the frequency response of the system. Figure 8 shows the frequency data for a range of forcing values, where lighter yellow colors indicate more content at that frequency. These plots were generated by solving the time histories at each Λ value with initial conditions of a small modal deflection in each mode. A Fast Fourier Transform (FFT) was performed and the data was scaled to the largest peak in the FFT, such that at each Λ value, the colormap scales from 0 to 1. These figures show the standard expected result, that the first and second frequencies coalesce to form a flutter response. It is interesting to note that the value of θ does not significantly change this phenomenon, however at high angles of θ ° and θ ° there is far less content in the second mode than in the first mode. Furthermore, at lower angles, there is more frequency content between the first and second frequencies when $\theta = 0$ ° and more content between the second and third frequencies when $\theta = 4$ °. Overall, at each angle, the first and second modes coalesce to form flutter, although the flutter point is decreased slightly with increasing angle, and the frequency content at subcritical forcing levels is changed somewhat substantially at higher angles.

Lastly, we can evaluate flap effectiveness by computing the moment on the hinge and comparing to a perfectly rigid flap. By defining flap effectiveness as

$$E_f = \frac{M(flexible)}{M(rigid)} \tag{53}$$

we can quantify the loss of control authority to the flexibility of the flap. Figure 9 illustrates this phenomena by plotting flap effectiveness for a range of pre-flutter pressure ratios and a selection of initial control surface rotations. It is interesting to note that for all rotation values, the effectiveness is similar, especially considering the differences in deflection illlustrated in Fig. 7. By plotting up to each case's flutter point, we reveal another interesting trend, that the effectiveness just before the flutter point of each rotation is remarkably similar, about 7.5%. Obviously this plate is much more flexible than a typical control surface, but the conclusion that flap effectiveness can be an indicator of aeroelastic stability may be significant more generally.



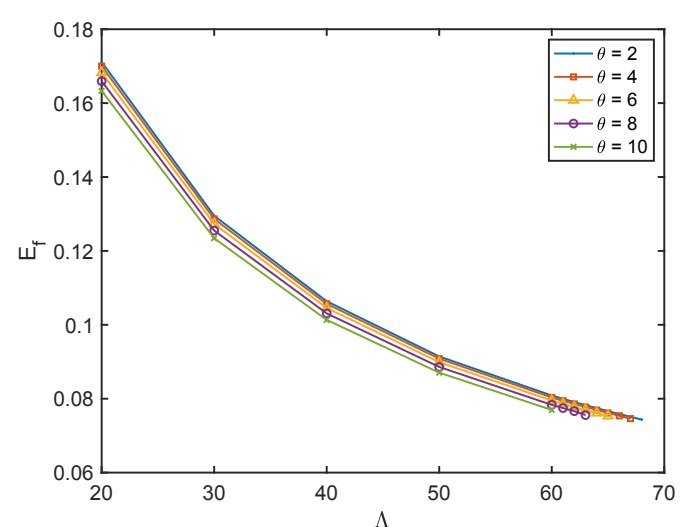


Figure 9: Flap effectiveness versus pre-flutter pressure ratio for various control surface rotations. Note that each line stops at its respective flutter boundary, and that the flap effectiveness is remarkably similar across rotation cases.

4 CONCLUSION

Here we have presented a new mathematical model which predicts the behavior of a simplified trailing edge control surface in high speed flow. A flexible plate represents a torsion-free flap as it rotates about a hinged corner. Oblique waves at the corner generate a steady pressure differential across the plate, and an enhanced piston theory predicts unsteady pressure across the flexible surface. The model was used to predict pre and post flutter dynamics as well as flap effectiveness relative to a perfectly rigid plate.

The results depict three types of sensitivity: Type 1, the sensitivity to the mathematical model of the physical system; Type 2, the sensitivity to the parameters within the model; and Type 3, the sensitivity to numerical methods. Type 1 sensitivity was studied by measuring the impact of including various nonlinearities. It was found that the model is most sensitive to the structural inertia and the third order piston theory nonlinearities. In other words, if the analysis did not include these mathematical terms, the solutions would differ greatly. Type 2 sensitivity was studied by varying Mach number and angle of rotation θ . Higher Mach numbers lead to larger LCO amplitudes, owing to the nonlinear piston theory terms. Increasing the rotation angle increases the model's sensitivity to second order piston theory terms, increases the static deflection of the plate, and decreases the critical pressure ratio. Type 3 sensitivity was accounted for by completing a modal convergence study, where it was found that 4 structural modes are sufficient for the range of parameters studied.

The flap effectiveness was measured by calculating the moment on the hinge for each steady displacement, and comparing this to the moment on a hinge due to a rigid plate. Considering the highly flexible plate in this study, it is not surprising that the effectiveness is rather low. This may also explain why this quantity is relatively insensitive to rotation angle θ . However it is interesting that the flutter point of various control surface rotation cases occurs at similar flap effectiveness levels, indicating that flap effectiveness may be an indicator of stability.

Future work includes a comparison to an Euler CFD solver to evaluate the inviscid pressure solution predicted by piston theory. A comparative Euler solution would validate the use of this computationally efficient method. This has been done in prior work for the special case of no control surface angle of attack. A step further is to model the structure with a higher fidelity method such as the finite element method, and couple this to a CFD solution. This would require sophisticated mesh deformation techniques, a nonlinear finite element model, and CFD; a recipe for extremely high computational time. It is also desirable to study this case experimentally.

5 APPENDIX A: PHYSICAL MODEL PARAMETERS

The model parameters were chosen based on measurements and specifications of the AFRL Research Cell 19 (RC-19) wind tunnel facility [1, 18]. However, it is important to note that a formal design study was not conducted. The flow parameters chosen are as follows.

$$M_{\infty} = 2$$

$$T_{\infty} = 288K$$

$$p_{\infty} = 100000Pa$$

$$R = 287J/(kgK)$$

$$\gamma = 1.4$$

The structural parameters are for a rectangular plate made of aluminum as follows.

$$b = 0.01m$$

$$L = 0.04m$$

$$\rho = 2700 kg/m^3$$

$$E = 70e9Pa$$

6 REFERENCES

- [1] S. Michael Spottswood, Timothy J. Beberniss, Thomas G. Eason, Ricardo A. Perez, Jeffrey M. Donbar, David A. Ehrhardt, and Zachary B. Riley. Exploring the response of a thin, flexible panel to shock-turbulent boundary-layer interactions. *Journal of Sound Vibration*, 443:74–89, Mar 2019.
- [2] Maxim Freydin, Earl H. Dowell, Thomas J. Whalen, and Stuart J. Laurence. A theoretical computational model of a plate in hypersonic flow. *Journal of Fluids and Structures*, 93:102858, 2020.
- [3] Gaetano M. D. Currao, Andrew J. Neely, Christopher M. Kennell, Sudhir L. Gai, and David R. Buttsworth. Hypersonic fluid–structure interaction on a cantilevered plate with shock impingement. *AIAA Journal*, 57(11):4819–4834, 2019.
- [4] Gaetano MD Currao, Andrew J Neely, David R Buttsworth, and Sudhir L Gai. Hypersonic fluid-structure interaction on a cantilevered plate. EUCASS, 2017.
- [5] K.A. McHugh, M. Freydin, K. Kruger Bastos, B. Beran, and E.H. Dowell. Flutter and limit cycle oscilations of cantilevered plate in supersonic flow. *Journal of Aircraft*, 2020. In press.
- [6] D. Tang, M. Zhao, and E.H. Dowell. Inextensible beam and plate theory: Computational analysis and comparison with experiment. *Journal of Applied Mechanics*, 81(6), 2014.
- [7] D. Tang, S.C. Gibbs, and E.H. Dowell. Nonlinear aeroelastic analysis with inextensible plate theory including correlation with experiment. *AIAA Journal*, 53(5):1299–1308, 2015.
- [8] E.H. Dowell and K.A. McHugh. Equations of motion for an inextensible beam undergoing large deflections. *Journal of Applied Mechanics*, 83:051007, 2016.
- [9] M. Raviv Sayag and E.H. Dowell. Linear versus nonlinear response of a cantilevered beam under harmonic base excitation: Theory and experiment. *Journal of Applied Mechanics*, 83:101002, 2016.
- [10] K.A. McHugh and E.H. Dowell. Nonlinear responses of inextensible cantilever and free-free beams undergoing large deflections. *Journal of Applied Mechanics*, 85:051008, 2018.
- [11] Kevin A McHugh and Earl H Dowell. Nonlinear response of an inextensible, cantilevered beam subjected to a nonconservative follower force. *Journal of Computational and Nonlinear Dynamics*, 14(3):031004, 2019.
- [12] J.D. Anderson. *Fundamentals of Aerodynamics*. Aeronautical and Aerospace Engineering Series. McGraw-Hill, 2001.
- [13] A.H. Shapiro. *The Dynamics and Thermodynamics of Compressible Fluid Flow, Volume 1.* Engineering special collection. Wiley, 1953.
- [14] M.J. Lighthill. Oscillating airfoils at high mach number. *Journal of the Aeronautical Sciences*, 20:402–406, 1953.
- [15] Holt Ashley and Garabed Zartarian. Piston theory-a new aerodynamic tool for the aeroelastician. *Journal of the Aeronautical Sciences*, 23:1109–1118, 1956.

- [16] Earl H. Dowell et al. A Modern Course in Aeroelasticity. Springer, New York, 2015.
- [17] Jack J. McNamara, Andrew R. Crowell, Peretz P. Friedmann, Bryan Glaz, and Abhijit Gogulapati. Approximate modeling of unsteady aerodynamics for hypersonic aeroelasticity. *Journal of Aircraft*, 47:1932–1945, 2010.
- [18] M.R. Gruber and A.S. Nejad. Development of a large-scale supersonic combustion research facility. AIAA 94-0544, 1994.